

# Modular Hybrid Plasmonic Integrated Circuit – Rotation, Nanofocusing and Nonlinear Enhancement

Alessandro Tuniz,<sup>1,2,\*</sup> Oliver Bickerton,<sup>1</sup> Fernando J. Diaz,<sup>1</sup> Thomas Käsebier,<sup>3</sup>  
Ernst-Bernhard Kley,<sup>3</sup> Stefanie Kroker,<sup>4,5</sup> Stefano Palomba,<sup>1,2</sup> and C. Martijn de Sterke<sup>1,2</sup>

<sup>1</sup>*Institute of Photonics and Optical Science, School of Physics, The University of Sydney, NSW 2006 Australia*

<sup>2</sup>*The University of Sydney Nano Institute, The University of Sydney, NSW 2006, Australia*

<sup>3</sup>*Institute of Applied Physics, Abbe Center of Photonics,*

*Friedrich Schiller Universität Jena, Max-Wien-Platz 1, 07743 Jena, Germany*

<sup>4</sup>*Physikalisch-Technische Bundesanstalt, Bundesallee 100, 38116 Braunschweig, Germany*

<sup>5</sup>*Technische Universität Braunschweig, LENA Laboratory for Emerging Nanometrology,  
Pockelsstrasse 14, 38106 Braunschweig, Germany*

(Dated: November 29, 2021)

We introduce a modular approach for efficiently interfacing photonic integrated circuits with deep-sub-wavelength hybrid plasmonic functionality. We demonstrate that an off-the-shelf silicon-on-insulator waveguide can be post-processed into an integrated hybrid plasmonic circuit by evaporating a silica and gold nanolayer. The circuit consists of a plasmonic rotator and a nanofocuser module, which together result in nano-scale, nonlinear wavelength conversion. We experimentally characterize each module, and demonstrate an intensity enhancement of  $> 200$  in a calculated mode area of  $50 \text{ nm}^2$  at  $\lambda = 1320 \text{ nm}$  using second harmonic generation. This work opens the door to customized plasmonic functionalities on industry-standard waveguides, bridging conventional integrated photonic circuits with hybrid plasmonic devices. This approach promises convenient access to nanometre-scale quantum information processing, nonlinear plasmonics, and single-molecule sensing.

## INTRODUCTION

Chip-based nanophotonic waveguides that incorporate photonic and electronic functionality on a compact, monolithic platform [1] promise to revolutionize communications, sensing, and metrology [2–4]. The most promising approach being pursued relies on expanding existing silicon-on-insulator (SOI) technologies from the electronic to the optical domain, to produce photonic integrated circuits (PICs) exhibiting superior performance in terms bandwidth and speed [5, 6]. The quest for optical miniaturization is ultimately limited by diffraction – which in silicon corresponds to a maximum achievable spatial confinement of approximately  $200 \text{ nm}$  at telecommunication wavelengths. One of the most promising approaches for beating the diffraction limit by several orders of magnitude relies on nano-plasmonic structures [7], which harness metals to compress light down to the molecular, and even atomic scale [8, 9]. Moreover, the giant intensity enhancement provided by plasmonic nanofocusing – typically  $\sim 100$ – $2000$  times [10] – has attracted interest for ultrafast, high-bandwidth, low-power nonlinear optics applications [11, 12], e.g., for nano-scale sensing [13] and all-optical wavelength conversion [14]. Plasmonics can be harnessed for nanoscale second- and third- harmonic generation, which respectively relied on either the large surface  $\chi^{(2)}$  or bulk  $\chi^{(3)}$  of the metal itself [15–17], or on the large intensity enhancement within a dielectric at a plasmonic nanofocus [14]. This has mainly been demonstrated in planar structures that cannot be efficiently interfaced to PICs [18].

Interfacing waveguide-based PICs with plasmonic nanostructures is challenging: typically, the latter are hindered by large losses (due to metallic absorption) and low coupling efficiency (due to extreme differences in the participating mode profiles). PICs and plasmonics can be married using hybrid plasmonic waveguides (HPWGs) containing a low-index buffer layer between the metal and the high-index waveguide, enabling relatively low propagation loss without sacrificing plasmonic confinement, and providing a convenient intermediate interface for coupling between photonic and plasmonic waveguides [19, 20]. Whereas the efficient energy transfer between PIC-compatible photonic- and plasmonic- structures has been under intense experimental investigation with a diverse range of functionality [21–25], including HPWG experiments demonstrating tight confinement and low propagation losses [26–28], nonlinear experiments using this platform have been limited [29].

While a number of simple HPWGs have been reported, the next challenge is to incorporate them into a more complex circuit with multiple modular, functional elements – analogously to conventional PICs [1]. Ideally, such structures

---

\* alessandro.tuniz@sydney.edu.au

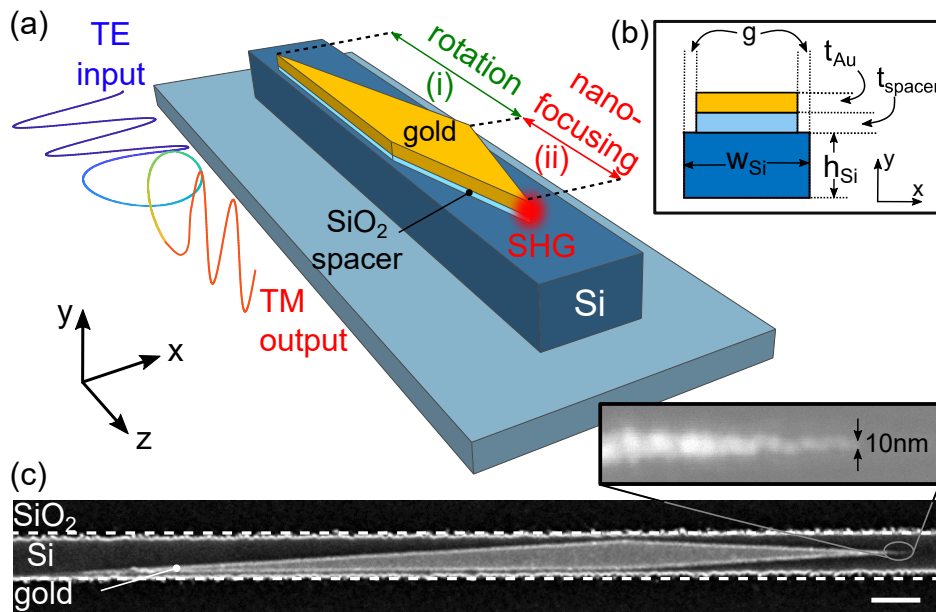


FIG. 1. (a) Schematic of our SOI-HPIC. It consists of an industry-standard TE ridge waveguide followed by two in-series plasmonic circuit modules: (i) efficient TE-photonic to TM-plasmonic rotator, and (ii), nano-focusing tip. (b) Geometric parameters at the rotator-focuser boundary. (c) Scanning electron micrograph (SEM) of a fabricated device. Scale bar: 400 nm. Here,  $w_{\text{Si}} = 350$  nm;  $h_{\text{Si}} = 220$  nm;  $g = 25$  nm;  $t_{\text{spacer}} = 20$  nm;  $t_{\text{Au}} = 50$  nm. Inset: high resolution nanotip detail, revealing 10 nm apex sharpness.

would be entirely chip-based, and be accessible using standard, industry-norm photonic components, thus simplifying the integration with more conventional technologies. Here we present, for the first time, the design, fabrication, and characterization of such a circuit, operating at  $\lambda = 1.32 \mu\text{m}$ . It consists of two modules: a mode converter that efficiently transforms an incoming photonic transverse electric (TE) mode into a hybrid-plasmonic transverse magnetic (TM) mode, followed by a plasmonic nanofocuser that functions as a nonlinear wavelength converter. We note that standard solutions exist for the coupling of light into the TE photonic waveguide, which here is achieved by using a grating with an incident free-space Gaussian beam. In this way, our device thus represents a fully integrated chip by which a free-space Gaussian beam is focussed to a cross-section that is almost two orders of magnitude below the diffraction limit in silicon, with a concomitant increase in intensity. To demonstrate that this increased intensity is due to the focuser, we fabricate and characterize two similar devices: one with a partial focuser and one with no focusing element at all.

Note that while preliminary reports of both a TE-to-TM rotator [30] and directional-coupling-based TM-nanofocuser [28] have been reported separately, this is the first proposal and demonstration of combining these two modular elements into a monolithic PIC-compatible plasmonic integrated circuit. This approach has clear advantages in terms of both design flexibility (enabling an industry-standard TE-waveguide input to achieve plasmonic nanofocusing), and wider bandwidth (enabled by the adiabatic modal evolution).

## RESULTS

### Circuit Design

Our on-chip hybrid plasmonic integrated circuit (HPIC) is formed by two in-series plasmonic elements on a SOI waveguide (WG): a mode converter and a focuser. The latter combines a taper and a sharp tip, which functions as a nonlinear nanoscale light source. In our particular demonstration we probe second harmonic generation (SHG) in the visible from a near-infrared pump. Figure 1(a) shows a schematic of the HPIC. The first component (i) is formed by a polarization rotator [30] (also operating as a TE-photonic to TM-plasmonic mode converter [31]); the second (ii) is a nanofocusing gold tip [10] resulting in SHG due to the intense nanoscale localization of the optical field, combined with the large surface  $\chi^{(2)}$  of gold [18]. Figure 1(c) shows an electron micrograph of a fabricated HPIC on a SOI waveguide, highlighting the  $\sim 10$  nm tip sharpness, which is limited only by the gold grains generated during the evaporation process [32].

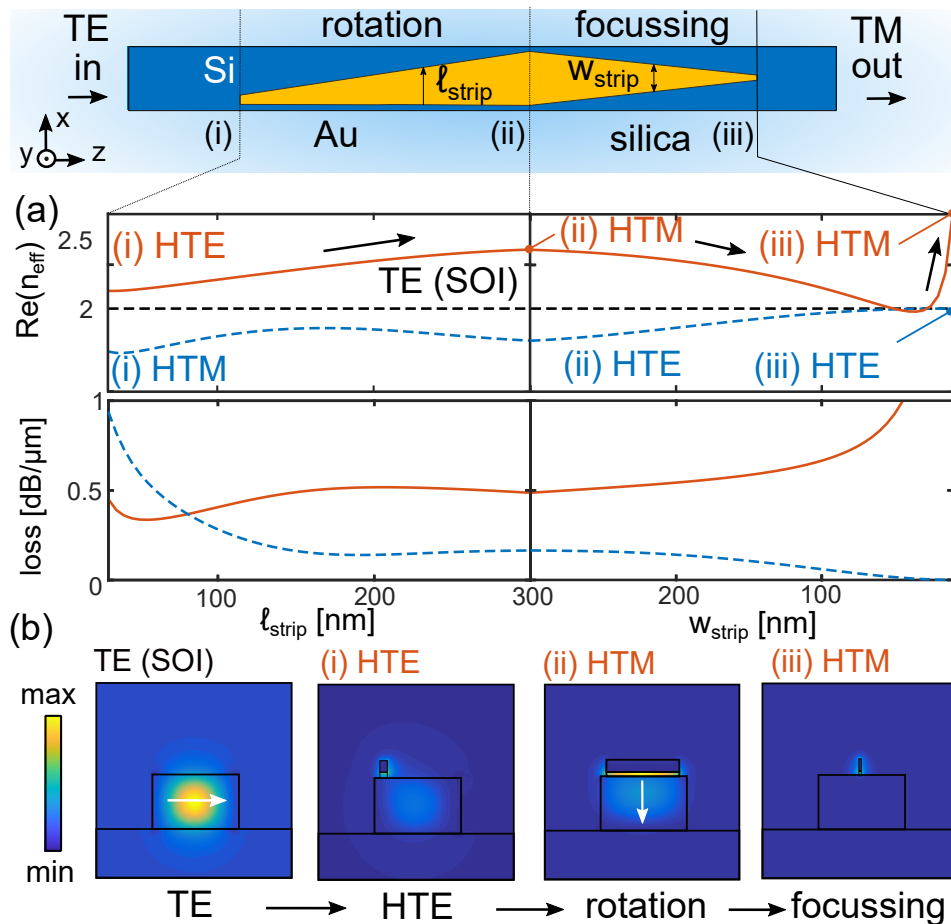


FIG. 2. (a) Calculated effective index  $\Re(n_{\text{eff}})$  and loss for relevant modes ( $\lambda = 1.32 \mu\text{m}$ ). Red line: a TE mode at input (TE SOI) (i) couples to a hybrid TE (HTE) mode, (ii) evolving to a rotated hybrid TM (HTM) mode, and (iii) transitions to a nano-focussed HTM plasmonic mode. The dashed blue line shows the HTM-to-HTE evolution. (b) Corresponding mode profiles as labelled. White arrows represent the dominant electric field direction. Window size:  $0.8 \times 0.8 \mu\text{m}^2$ . See Fig. 1 caption for relevant parameters.

To analyze our circuit we first consider the relevant HPIC modes during propagation. Figure 2(a) shows the result of 2D finite element (FE) simulations (COMSOL) of the modal evolution along the HPIC. Figure 2(a) also shows a top-view schematic of Fig. 1 for clarity. In first instance, a gold film [33] ( $t_{\text{Au}} = 50 \text{ nm}$ ) with a  $\text{SiO}_2$  spacer underneath [34] ( $t_{\text{spacer}} = 20 \text{ nm}$ ) gradually extends on a silicon waveguide ( $350 \text{ nm} \times 220 \text{ nm}$ ,  $n_{\text{Si}} = 3.5$ ) until complete coverage (here,  $\ell_{\text{strip}} = 30 - 300 \text{ nm}$ ). The red line in Figure 2(a) shows how the hybrid-TE (HTE) mode evolves within the waveguide, in terms of the real effective index and loss. The input is the fundamental TE-SOI mode of the bare waveguide, which excites the HTE mode (i) that rotates into a hybrid-TM mode (HTM) (ii). The HTM mode is then converted to a deep-subwavelength HTM plasmonic mode (iii) [35] by reducing the gold strip width ( $w_{\text{strip}} = 300 - 10 \text{ nm}$ ). The Poynting vector associated with each participating mode is shown in Fig. 2(b), and presents the salient features of the evolution of TE-SOI mode after it couples to the HTE mode. The modal evolution of the equivalent HTM mode is shown as the blue curve in Fig. 2(a) for completeness. The TE-SOI waveguide mode excites both the HTE and HTM hybrid plasmonic eigenmodes in location (i), each evolving in a non-trivial way along the device.

We next calculate the performance of the full device using full 3D FE simulations. Due to the many parameters, materials, and functionalities involved, the optimization of the complete device is challenging: first, a suitable compromise between adiabaticity (requiring a slow modal transition, i.e., a long device length) and loss (requiring short device lengths) is required; secondly, small changes in geometric parameters, alignment, and surface roughness can have significant impact on the conversion efficiency. However, this process can be significantly simplified by using the modularity, which enables us to consider each element separately. In line with previous designs [30, 35] and to demonstrate a proof of concept, we have chosen the rotator length to be  $6 \mu\text{m}$ , and the focusser length to be  $3 \mu\text{m}$ , which by no means represent a fully optimized structure.

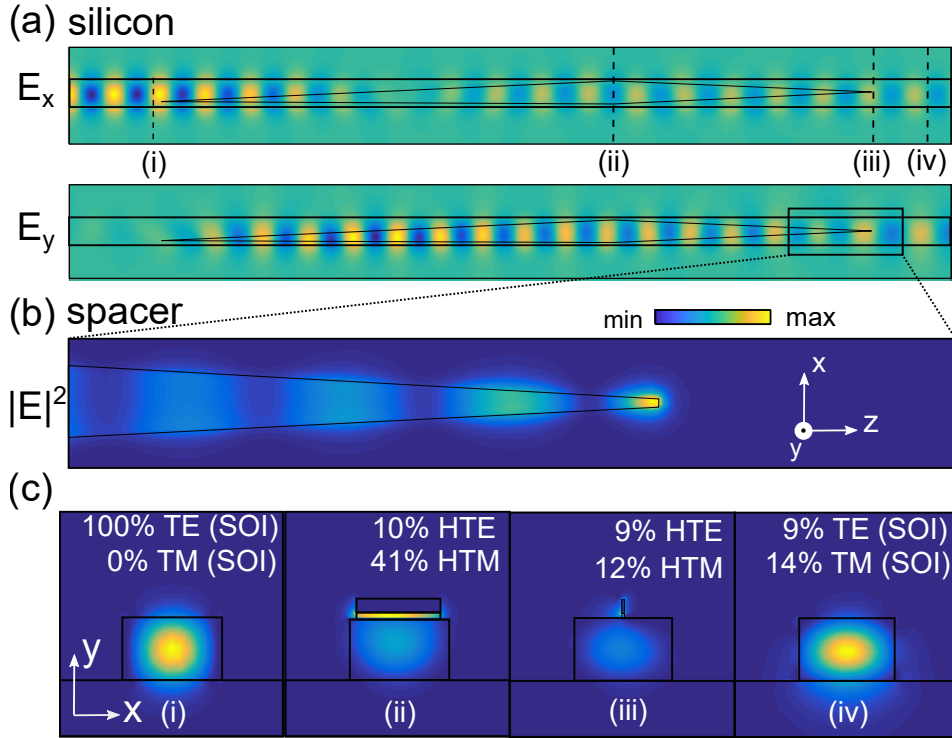


FIG. 3. 3D FE simulations of device performance. (a) Electric field in the  $xy$  plane (a) in the middle of the silicon waveguide, showing polarization rotation. Window size:  $7 \times 1 \mu\text{m}^2$ . (b) Field intensity  $|\mathbf{E}|^2$  in the middle of the spacer, showing nano-concentration of energy. Window size:  $1.5 \times 0.2 \mu\text{m}^2$ . (c) Time-averaged power flow at each of the locations (i)–(iv) as labelled in (a). Inset: relative contribution (in %) for each mode shown in Fig. 2 [31].

We model the fabricated structure shown in Fig. 1(c). The cross-section of the  $E_x$  and  $E_y$  field components in the middle of the Si-WG are shown in Fig. 3(a). Note in particular the polarization rotation in the spacer, manifesting as a vanishing  $E_x$  component and an emerging  $E_y$  component. A detailed plot of the electric field intensity within the spacer near the tip is shown in Fig. 3(b), showing a strong local enhancement at the tip apex. We calculate a  $\sim 1200\times$  intensity enhancement at the gold surface with respect to the peak intensity in the silicon for the TE-SOI input. Figure 3(c) shows the power in each  $xy$  cross section as indicated by the dashed lines in Fig. 3(a)(i)–(iv). We calculate the conversion efficiency between the incoming TE-SOI mode and each of the participating modes in the full device by performing overlap integrals between the calculated 3D fields of Fig. 3(c) and the 2D modes of Fig. 2, as outlined in Ref. [31]. We obtain a TE-to-HTM (rotator) conversion efficiency of 41%, comparable to previous reports [30]), and a TE-to-HTM (nanofocus) conversion efficiency of 12%, also comparable to the state of the art for plasmonic nanofocusing [14]. Note that 9% of the TE mode remains in the WG at output, which can be improved, for example, by more sophisticated multi-section rotator designs [36].

### Fabrication and Linear Experiments

With an eye on the potential for modular approach to enhance off-the-shelf photonic waveguides with tailored plasmonic functionality, we purposefully choose to integrate our HPICs on previously fabricated SOI-WGs with standard electron-beam lithography and evaporation techniques. Figure 4 shows a microscope image of an example bare SOI-WG with length  $L = 20 \mu\text{m}$ : light is coupled in- and out- of the waveguide with shallow gratings optimized for TE polarization. For further details of the bare SOI-WG design and characterization, see Methods and Supplementary Material. The HPIC nanostructures, shown in Fig. 1(c), were deposited on the WG in a subsequent step via combination of electron-beam lithography,  $\text{SiO}_2$ /gold evaporation, and lift-off – note in particular the excellent quality of the gold film, the sharp tip obtained, and the high alignment precision ( $< 10 \text{ nm}$  resolution). The details of the HPIC fabrication procedure are presented in the Methods and in Supplementary Material. Preliminary experimental waveguide characterization in the near-infrared (NIR) was performed by coupling light from free space ( $\lambda = 1320 \mu\text{m}$ ) onto the waveguide input grating coupler using a  $100\times$  near-infrared microscope objective (NA = 0.85 - Olympus) and

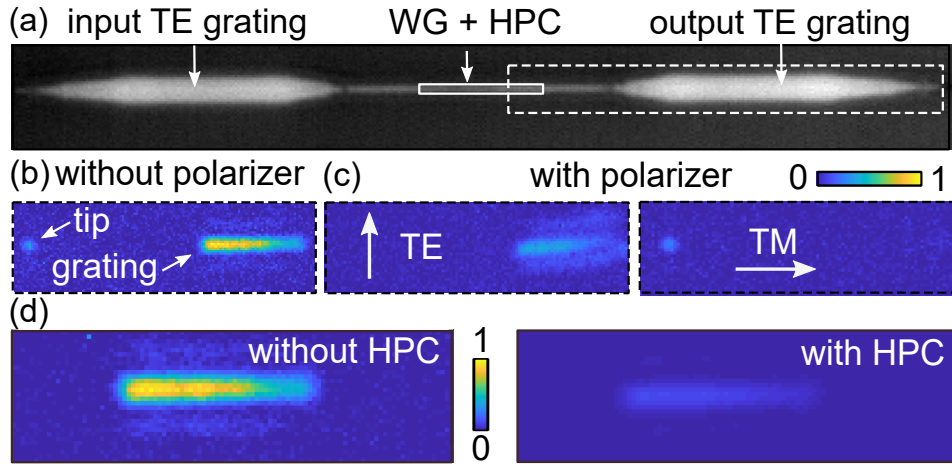


FIG. 4. (a) Microscope image of a  $20\ \mu\text{m}$  WG with an HPIC (SEM inset). Light is coupled to the waveguide using a TE grating at input. (b) Measured light from the output TE grating and the tip (dashed line in (a)). (c) Placing a polarizer between scattered light and camera confirms that light from the tip is TM polarized, while light from the grating is TE polarized. White arrows in (c) show polarizer orientation. (d) Measured light scattered by the output grating with- and without- the HPIC, resulting in 12% relative transmittance.

observing the light scattered by the device using a InGaAs camera (NIRvana, Princeton Instruments) (see Methods and Supplementary Material). The resulting measurement is shown in Fig. 4(b): we observe a diffraction-limited nanospot at the expected location of the gold nanotip, as well as residual TE light contained within the waveguide (in agreement with the simulations, see Fig. 3(a)(iv)), originating from the output grating. Figure 4(c) shows the same measurement when inserting a polarizer between the sample and camera with different orientations: we measure that the diffraction-limited spot is longitudinally (TM) polarized [37], confirming polarization rotation and that light exiting the grating is TE polarized. As further confirmation, Fig. 4(d) shows a direct comparison of the amount of light exiting the grating in the presence of the HPIC, with respect to an adjacent control sample without the HPIC. From the ratio of the total power scattered by each TE grating under comparable input conditions (see Supplementary Material), we conclude that the residual light in the TE waveguide in the presence of the HPIC, relative to the bare SOI waveguide, is  $(13 \pm 1)\%$ , in agreement with 3D simulations (see Fig. 3(c)(iv)).

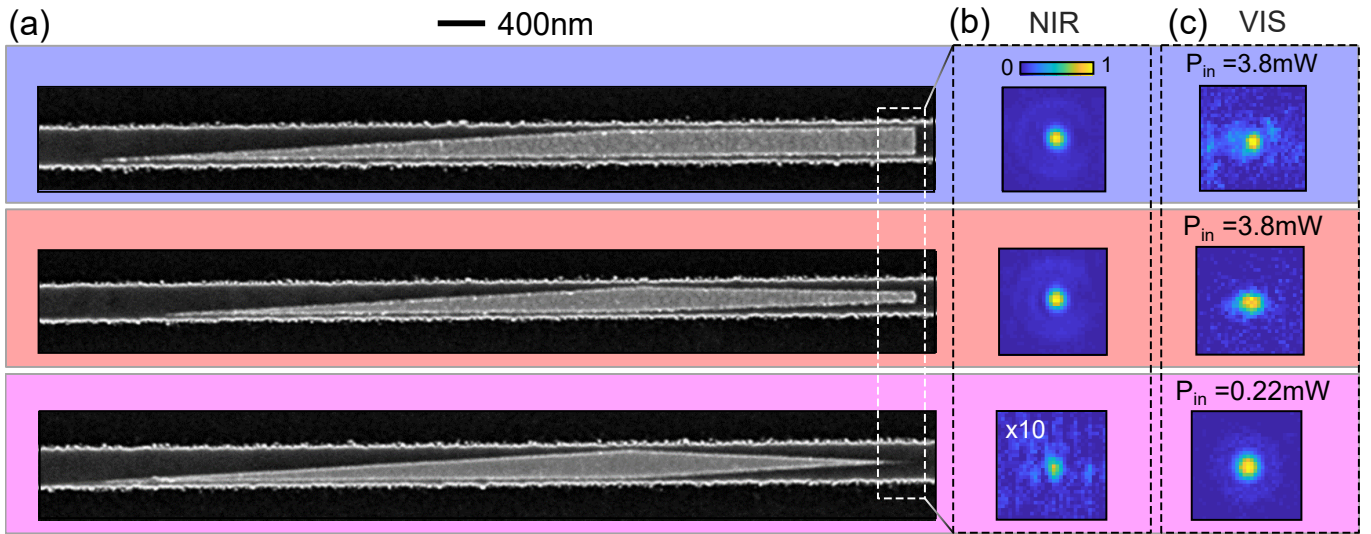


FIG. 5. (a) SOI-HPIC scanning electron micrographs, with tip width of 300 nm (blue), 138 nm (red) and 10 nm (magenta). Measured scattering from the SOI-HPIC at (b) in the NIR (c) and visible. Images in (b), (c) are respectively captured under the same conditions, unless otherwise indicated.  $P_{\text{in}}$  is the average power incident onto the input grating for the three captured images in (c). respectively.

### Nanofocusing and Nonlinear Enhancement

Plasmonic nanofocusing leads to spot sizes that are well below the diffraction limit, so that far-field linear optical experiments are inherently incapable of characterizing the focusing performance of our HPIC. Here we harness the high field intensities at the apex of the gold tip to estimate the field enhancement via nonlinear SHG experiments. Ultrashort pump pulses ( $\lambda_p = 1320$  nm, 200 fs, 80 MHz [29]) are coupled into the TE mode of the photonic waveguide via a grating coupler. They then enter one of three HPIC-enhanced WGs, each possessing increasingly sharper tips: the three HPIC considered here are shown in Fig. 5(a). Scattered light images by each HPIC captured using near-infrared (NIR) and visible (VIS) cameras (PIXIS – Princeton Instruments) are shown in Fig. 5(b) and 5(c), respectively. While nonlinear generation/scattering occurs during propagation across the entire HPIC [15], due to the large absorption of silicon (approximately 12 dB over 10  $\mu\text{m}$  at 660 nm [38]), the absence of phase matching, and the wavelength-scale propagation lengths considered, we can attribute the measured nonlinear signal only to the localized intensity at the edge of the gold tip from which the NIR light emerges. The spectra of the NIR pump and the visible radiation are shown in the inset of Fig. 6(a). The figure confirms that the visible radiation indeed is the second harmonic of the pump since  $\lambda_{\text{SHG}} = \lambda_p/2 = 660$  nm. We observe that the sharpest tip causes the least amount of NIR scattering, consistent with 3D simulations (see Supplementary Material). In contrast, this tip also causes the strongest visible light emission (see Fig. 5(b),(c), magenta), even though the incident power is an order of magnitude smaller than in the other two cases – a preliminary indicator of nonlinear enhancement. In this case the input power is reduced by 10 times in order to avoid damaging the sharp due to the high field strength.

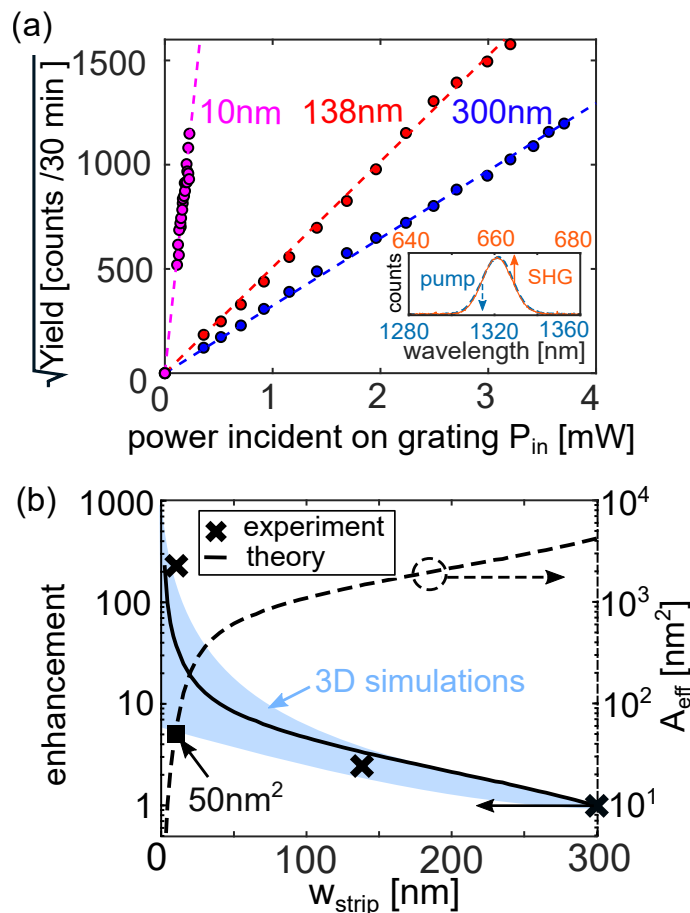


FIG. 6. Experimental demonstration of nanoscale intensity enhancement in the HPIC. (a) Circles: square root of the measured yield for each sample (colour coding as in Fig. 5). Dashed lines: linear fits confirming quadratic dependence on incident power ( $I_{\text{SHG}}^{1/2} \propto P_{\text{in}}$ ). Inset: spectra of the pump (blue), and of the SHG from the tip (orange). (b) Calculated enhancement (left axis, solid line) and effective area (right axis, dashed line) as a function of strip width, relative to the largest  $w_{\text{strip}} = 300$  nm, following Ref. [35]. Blue shadow encompasses enhancement values predicted by full 3D simulations, see Supplementary Material. Black crosses show the experimentally measured relative increase in intensity, obtained from the square of the slopes in (a). Black square: calculated effective area of 50 nm<sup>2</sup> for  $w_{\text{strip}} = 10$  nm.

To quantify the nonlinear response of each tip, we measure the raw spectral yield versus incident power at the SHG wavelength, as shown in Fig. 6(a) (circles). The linear relationship between the square root of the yield and the average power incident on the sample  $P_{\text{in}}$  (corresponding to a quadratic input power dependence,  $I_{\text{SHG}}^{1/2} \propto P_{\text{in}}$ ), further confirms the mechanism of SHG. As a first conclusion we note the dramatic increase in SHG intensity for the sharpest tip, which indicates that nano-focusing was achieved. We compare the slopes of the three curves quantitatively via a linear fit to the experiment, as shown in the dashed lines of Fig. 6(a), and infer the relative intensity enhancement with respect to the strip. The results are summarized in Fig. 6(b), which shows the intensity enhancement as a function of the tip width obtained using different approaches. Black crosses show the measured enhancement, obtained by taking the square of the slopes in (Fig. 6(a)), normalized to  $w_{\text{strip}} = 300$  nm. We experimentally observe a maximum intensity enhancement of  $\sim 220\times$  for the sharpest gold tip relative to the gold strip. The theoretical enhancement at the tip is shown as a solid line in Fig. 6(b) (left axis), and was calculated using an adiabatic Eikonal approach [35], in excellent agreement with both the experiment and the range of intensity enhancements at the tip predicted by full 3D simulations (light blue region – see Supplementary Material for further details). Based on these results, the inferred effective mode area is  $A_{\text{eff}} \sim 50 \text{ nm}^2$  [38] (black square).

Finally, we estimate the SHG conversion efficiency. After taking into account the effect of all optical elements, we conclude that the maximum SHG power is emitted by the sample for the sharpest nanotip (Fig. 6(a), magenta) is 2.3 fW for an incident power of 0.22 mW, corresponding to a net conversion efficiency of  $10^{-11}$ . Taking into account the coupling efficiency into the waveguide (14%, see Supplementary Material), this corresponds to  $\sim 0.7 \times 10^{-10}$  of the power in the waveguide before the plasmonic rotator, and  $\sim 0.6 \times 10^{-9}$  of the inferred power in the TM mode at the tip (cfr. Fig. 2(d)(ii)). Though these values are comparable to optimized nonlinear plasmonic SHG geometries [18, 39], our geometry has the significant advantage of being on a PIC-compatible platform. It is worth noting that only  $\sim 0.06\%$  of the power generated by a TM point source on the surface of a silicon waveguide radiates upwards, whereas the great majority of the SHG light is scattered into (and absorbed by) the silicon waveguide (see Supplementary Material). Future work will focus on new strategies to make use of the generated SHG, e.g., using hydrogenated amorphous silicon with low absorption at visible wavelengths, which will enable measurements of the SHG signal captured by the photonic waveguide [40].

## DISCUSSION

The conversion efficiency could be further improved by optimizing the individual modular elements. Separate calculations for each module predict a peak rotator conversion efficiency of 58% for a rotator length of  $4 \mu\text{m}$ , and of 34% for a focuser length of  $1 \mu\text{m}$  (keeping all other parameters constant), resulting in a compound conversion efficiency of 20%. This in good agreement with equivalent calculations for the full device, predicting a maximum conversion efficiency of 24% for the same rotator- and focuser lengths of  $4 \mu\text{m}$  and  $1 \mu\text{m}$ , respectively. Thus, we estimate that through modest changes of the device parameters (e.g., increasing the gold thickness or with multi-section tapers [36] with up to 95% conversion efficiency), the pump TE-to-TM efficiency could be improved by approximately  $9\times$ , which would lead to a  $\sim 80$ -fold increase in nonlinear conversion efficiency. Further improvements may be achieved either by incorporating 2D materials on the waveguide surface, which possess a  $\chi^{(2)}$  that is at least one order magnitude greater than gold surfaces [40]. Additionally,  $\chi^{(3)}$  nonlinear effects such as third harmonic generation and four-wave-mixing may be accessed by placing highly nonlinear materials at the nanofocus [14]. Further enhancement may be achieved with additional plasmonic modules, such as a bowtie nanoantenna [41] adjacent to the tip, or additional focuser and rotator modules which couple light back into the photonic waveguide.

This experiment represents the first PIC-compatible, integrated nonlinear-plasmonic-SHG nanoscale light source, that makes use of two, in-series hybrid-plasmonic circuit elements. This design, fabrication, and characterization represents the first TM plasmonic nano-focuser that is monolithically interfaced with an industry-standard TE-input SOI waveguide, and which can be coupled into by a conventional grating coupler. This work opens the door to the development of modular plasmonic circuit elements that can be seamlessly integrated on off-the-shelf photonic waveguides. This approach will facilitate access to efficient PIC-compatible deep-subwavelength field enhancements for on-chip quantum photonics and spectroscopy [42], nonlinear [13] and atomic-scale [9] sensing, and nanoscale terahertz sources and detectors [43].

## METHODS

### Photonic waveguide grating design and characterization

The waveguide gratings were designed in-house using a 2D solver CAMFR [44], with infinite air cladding and silicon substrate layer, a box layer of  $2\ \mu\text{m}$  thick, and a silicon waveguide layer of 220 nm, presenting grooves with an etching depth of  $h_e$  and a period of  $\Lambda$ . Here,  $h_e = 80\ \text{nm}$  and period  $\Lambda = 440\ \text{nm}$ , resulting in a high coupling efficiency ( $T_{\text{up}} = 51\%$ ), and wide bandwidth centered in  $\lambda = 1320\ \text{nm}$ , low reflection ( $R = 3.5\%$ ), and a selective in-coupling angle ( $-11^\circ$ ). From images of the optimized coupling to the waveguide, referenced to a mirror, we obtain a grating coupling efficiency of 14%, assuming that the loss due to each grating is equal. Waveguide losses without the HPIC are measured to be  $0.12\ \text{dB}/\mu\text{m}$  using waveguides of different lengths. See Supplementary Material for further details of the calculations, the calculated bandwidth, and experimental measurements of coupling- and propagation- losses.

### Hybrid plasmonic integrated circuit fabrication

The plasmonic HPICs are integrated on the SOI waveguides as follows. First, the silicon waveguides are spin-coated with PMMA resist, and the HPIC structures are written with standard electron-beam lithography (EBL) and developed with Methyl isobutyl ketone. 20 nm silica and 50 nm gold are subsequently coated with electron-beam evaporation. Finally, a lift-off step (Methyl-isobutyl-ketone) removes the resist. The alignment precision ( $\sim 10\ \text{nm}$ ) is obtained using local gold markers, placed in the immediate vicinity of our off-the-shelf waveguides. See Supplementary Material for a schematic of the fabrication procedure and alignment markers used.

### Experimental setup

A detailed schematic of the experimental setup is shown in Supplementary Material. The source is an Optical Parametric Oscillator (OPO) ( $\lambda_p = 1320\ \text{nm}$ , FWHM: 200 fs; repetition rate: 80 MHz). The power incident on the sample is controlled via a motorized half-waveplate (HWP) placed before a polarizer. The beam is spatially shaped using a beam expander, telescope, and elliptical lens, so that its profile matches that of the input waveguide grating. A beamsplitter ( $\text{BS}_{\text{PM}}$ ) and powermeter (PM) monitor the input power. A microscope holds the WGs and HPICs. Light is delivered and collected to the sample via a  $100\times$  NIR microscope objective (Olympus, NA = 0.85) and BS. A short-pass filter (850 nm) is included in SHG experiments to filter out the NIR light. The scattered light is measured with an imaging spectrometer, using NIR (NIRvana) and VIS (PIXIS) cameras. An additional NIR camera at a second output monitors alignment.

- 
- [1] L. Chrostowski and M. Hochberg, *Silicon photonics design: from devices to systems* (Cambridge U. Press, 2015).
  - [2] P. Dong, X. Liu, S. Chandrasekhar, L. L. Buhl, R. Aroca, and Y.-K. Chen, *IEEE Journal of Selected Topics in Quantum Electronics* **20**, 150 (2014).
  - [3] M. C. Estevez, M. Alvarez, and L. M. Lechuga, *Laser & Photonics Reviews* **6**, 463 (2012).
  - [4] D. Marpaung, J. Yao, and J. Capmany, *Nature Photonics* **13**, 80 (2019).
  - [5] M. Lipson, *Journal of Lightwave Technology* **23**, 4222 (2005).
  - [6] L. Chen, K. Preston, S. Manipatruni, and M. Lipson, *Optics Express* **17**, 15248 (2009).
  - [7] R. Zia, J. A. Schuller, A. Chandran, and M. L. Brongersma, *Materials Today* **9**, 20 (2006).
  - [8] A. B. Taylor and P. Zijlstra, *ACS Sensors* **2**, 1103 (2017).
  - [9] J. Lee, K. T. Crampton, N. Tallarida, and V. A. Apkarian, *Nature* **568**, 78 (2019).
  - [10] D. K. Gramotnev and S. I. Bozhevolnyi, *Nature Photonics* **4**, 83 (2010).
  - [11] M. Kauranen and A. V. Zayats, *Nature Photonics* **6**, 737 (2012).
  - [12] G. Li, C. M. de Sterke, and S. Palomba, *ACS Photonics* **5**, 1034 (2018).
  - [13] V. Kravtsov, R. Ulbricht, J. M. Atkin, and M. B. Raschke, *Nature Nanotechnology* **11**, 459 (2016).
  - [14] M. P. Nielsen, X. Shi, P. Dichtl, S. A. Maier, and R. F. Oulton, *Science* **358**, 1179 (2017).
  - [15] A. de Hoogh, A. Opheij, M. Wulf, N. Rotenberg, and L. Kuipers, *ACS Photonics* **3**, 1446 (2016).
  - [16] M. Celebrano, X. Wu, M. Baselli, S. Großmann, P. Biagioni, A. Locatelli, C. De Angelis, G. Cerullo, R. Osellame, B. Hecht, *et al.*, *Nature Nanotechnology* **10**, 412 (2015).
  - [17] J. B. Lassiter, X. Chen, X. Liu, C. Ciraci, T. B. Hoang, S. Larouche, S.-H. Oh, M. H. Mikkelsen, and D. R. Smith, *ACS Photonics* **1**, 1212 (2014).

- [18] J. Butet, P.-F. Brevet, and O. J. Martin, *ACS Nano* **9**, 10545 (2015).
- [19] R. F. Oulton, V. J. Sorger, D. Genov, D. Pile, and X. Zhang, *Nature Photonics* **2**, 496 (2008).
- [20] M. Z. Alam, J. S. Aitchison, and M. Mojahedi, *Laser & Photonics Reviews* **8**, 394 (2014).
- [21] R. M. Briggs, J. Grandier, S. P. Burgos, E. Feigenbaum, and H. A. Atwater, *Nano Letters* **10**, 4851 (2010).
- [22] C. Delacour, S. Blaize, P. Grosse, J. M. Fedeli, A. Bruyant, R. Salas-Montiel, G. Lerondel, and A. Chelnokov, *Nano Letters* **10**, 2922 (2010).
- [23] C. Lin, H. M. K. Wong, B. Lau, M. A. Swilam, and A. S. Helmy, *Applied Physics Letters* **101**, 123115:1 (2012).
- [24] A. Melikyan, L. Alloatti, A. Muslija, D. Hillerkuss, P. C. Schindler, J. Li, R. Palmer, D. Korn, S. Muehlbrandt, D. Van Thourhout, *et al.*, *Nature Photonics* **8**, 229 (2014).
- [25] C. Haffner, D. Chelladurai, Y. Fedoryshyn, A. Josten, B. Baeuerle, W. Heni, T. Watanabe, T. Cui, B. Cheng, S. Saha, *et al.*, *Nature* **556**, 483 (2018).
- [26] J. T. Kim, J. J. Ju, S. Park, M.-s. Kim, S. K. Park, and S.-Y. Shin, *Optics Express* **18**, 2808 (2010).
- [27] V. J. Sorger, Z. Ye, R. F. Oulton, Y. Wang, G. Bartal, X. Yin, and X. Zhang, *Nature Communications* **2**, 331 (2011).
- [28] Y. Luo, M. Chamanzar, A. Apuzzo, R. Salas-Montiel, K. N. Nguyen, S. Blaize, and A. Adibi, *Nano Letters* **15**, 849 (2015).
- [29] F. Diaz, T. Hatakeyama, J. Rho, Y. Wang, K. O'Brien, X. Zhang, C. M. de Sterke, B. Kuhlmeier, and S. Palomba, *Optics Express* **24**, 545 (2016).
- [30] J. N. Caspers, J. S. Aitchison, and M. Mojahedi, *Optics Letters* **38**, 4054 (2013).
- [31] S. Kim and M. Qi, *Optics Express* **23**, 9968 (2015).
- [32] I. Doron-Mor, Z. Barkay, N. Filip-Granit, A. Vaskevich, and I. Rubinstein, *Chemistry of Materials* **16**, 3476 (2004).
- [33] P. D. Johnson and R. W. Christy, *Physical Review B* **6**, 4370 (1972).
- [34] I. Malitson, *Journal of the Optical Society of America* **55**, 1205 (1965).
- [35] L. Lafone, T. P. Sidiropoulos, and R. F. Oulton, *Optics Letters* **39**, 4356 (2014).
- [36] Y.-J. Chang and R.-W. Feng, *Applied Optics* **56**, 5501 (2017).
- [37] A. Tuniz, M. Chemnitz, J. Dellith, S. Weidlich, and M. A. Schmidt, *Nano Letters* **17**, 631 (2017).
- [38] D. E. Aspnes and A. Studna, *Physical Review B* **27**, 985 (1983).
- [39] Y. Zhang, N. K. Grady, C. Ayala-Orozco, and N. J. Halas, *Nano Letters* **11**, 5519 (2011).
- [40] H. Chen, V. Corboliou, A. S. Solntsev, D.-Y. Choi, M. A. Vincenti, D. De Ceglia, C. De Angelis, Y. Lu, and D. N. Neshev, *Light: Science & Applications* **6**, e17060 (2017).
- [41] F. Peyskens, A. Dhakal, P. Van Dorpe, N. Le Thomas, and R. Baets, *ACS Photonics* **3**, 102 (2015).
- [42] M. S. Tame, K. McEnery, Ş. Özdemir, J. Lee, S. Maier, and M. Kim, *Nature Physics* **9**, 329 (2013).
- [43] Y. Salamin, W. Heni, C. Haffner, Y. Fedoryshyn, C. Hoessbacher, R. Bonjour, M. Zahner, D. Hillerkuss, P. Leuchtman, D. L. Elder, *et al.*, *Nano Letters* **15**, 8342 (2015).
- [44] D. Taillaert, F. Van Laere, M. Ayre, W. Bogaerts, D. Van Thourhout, P. Bienstman, and R. Baets, *Japanese Journal of Applied Physics* **45**, 6071 (2006).

## ACKNOWLEDGMENTS

A.T. acknowledges support from the University of Sydney Fellowship Scheme. S.K. acknowledges support by the German Research Foundation (DFG) under Germanys Excellence Strategy EXC-2123/1. This work was performed in part at the NSW node of the Australian National Fabrication Facility (ANFF).

## AUTHOR CONTRIBUTIONS

A.T. conceived the idea and designed the experiment with input from S.P. and C.M.d.S. A.T. performed the simulations, experiments, and fabrication of the hybrid plasmonic circuit. O.B. designed the plasmonic device and fabricated the alignment markers. F.J.D. designed the bare silicon waveguides and the experimental setup. T.K., S.K. and E-B.K. fabricated the bare waveguides. A.T. and C.M.d.S wrote the manuscript with input from S.P. A.T., C.M.d.S. and S.P. directed the project.